Improving the representation of shallow cumulus convection with the Simplified Higher-Order Closure Mass-Flux (SHOC+MF v1.0) approach

Maria J. Chinita[1,2], Mikael Witte[1,2,3], Marcin J. Kurowski[1], Joao Teixeira[1,2], Kay Suselj[1,6], Georgios Matheou[4], and Peter Bogenschutz[5]

[1] Jet Propulsion Laboratory, California Institute of Technology, Pasadena, California, USA
[2] Joint Institute for Regional Earth System Science and Engineering, University of California Los Angeles, Los Angeles, California, USA
[3] Naval Postgraduate School, Monterey, California, USA
[4] University of Connecticut, Storrs, Connecticut, USA
[5] Lawrence Livermore National Laboratory, Livermore, California, USA
[6] Running Tide Technologies, Inc, USA

Correspondence to: Maria J. Chinita (maria.j.chinita.candeias@jpl.nasa.gov)

Abstract. Parameterized boundary layer turbulence and moist convection remain some of the largest sources of uncertainty in general circulation models. High-resolution climate modeling aims to reduce that uncertainty by explicitly attempting to resolve deep moist convective motions. An example of such a model is the Simple Cloud-Resolving E3SM Atmosphere Model (SCREAM) with a target global resolution of 3.25 km, allowing for a more accurate representation of complex mesoscale deep convective dynamics. Yet, small-scale planetary boundary layer turbulence and shallow convection still need to be parameterized, which in SCREAM is accomplished through the TKE-based Simplified Higher-Order Closure (SHOC)—a simplified version of the assumed doubled-Gaussian PDF higher-order closure method. In this paper, we implement a stochastic multiplume Mass-Flux (MF) parameterization of dry and shallow convection in SCREAM to go beyond the limitations of double-Gaussian PDF closures and couple it to SHOC (SHOC+MF). The new parameterization implemented in a single-column model type version of SCREAM produces results for two shallow cumulus convection cases (marine and continental shallow convection) that agree well with the reference large-eddy simulation data, thus improving the general representation of the thermodynamic quantities and their turbulent fluxes as well as cloud macrophysics in the model. Furthermore, SHOC+MF parameterization shows weak sensitivity to the vertical grid resolution and model time step.

1 Introduction

In general circulation models (GCMs), subgrid physical processes need to be parameterized due to the typical horizontal resolutions of GCMs—$\mathcal{O}(10^2)$ km. Traditionally, the turbulent transport in the dry planetary boundary layer (PBL) is represented by a downgradient eddy-diffusivity approach sometimes combined with a countergradient flux term to account for the strong nonlocal transport in the dry convective boundary layer (CBL) (e.g., Deardorff 1966; Han and Pan 2011; Teixeira et al. 2004; Holtslag and Moeng 1991; Stevens 2000). For shallow cumulus, the transport is often represented by a separate cumulus parameterization based on the mass-flux approach (e.g., Betts 1973; Tiedtke 1989; Yoshimura et al. 2015; Beljaars et al. 2018). Such parameterizations often require cloud-base closures and trigger functions. This, combined with the standard GCM modular structure (i.e., GCMs

resort to several independent parameterizations to represent the transport that happens continuously in the real atmosphere), increases uncertainties and biases in GCMs (e.g., Teixeira et al. 2008; Sherwood et al. 2014; Schneider et al. 2017).

40   During the last two decades, unified parameterizations have been proposed and implemented in GCMs to reduce some of the issues associated with conventional modular approaches. Unified parameterizations aim to represent the continuous and evolving turbulent transport across the different PBL regimes, e.g., from dry to shallow cumulus convection, in a consistent manner. Two promising approaches emerged to unify boundary layer turbulence and moist convection: eddy-diffusivity mass-flux (EDMF) methods, and higher-order closures (HOCs) based on assumed probability density functions (PDFs). Examples of assumed PDFs
45   schemes include the Cloud Layers Unified By Binormals (CLUBB; Golaz et al. 2002), and Intermediately Prognostic Higher-Order Closure (IPHOC; Cheng and Xu 2006, 2008), where both schemes assume a double Gaussian PDF to represent subgrid-scale variability of vertical velocity, temperature, and moisture and, therefore, parameterize PBL turbulence and clouds. A key advantage of HOC-PDF schemes is that cloud macrophysical properties and higher-order moments are diagnosed from the joint PDF in a self-consistent manner. A critical downside is that most HOCs are usually computationally expensive as they require at
50   least seven prognostic equations for second and third-order moments depending on the chosen PDF. To reduce computational costs, the Simplified Higher-Order Closure (SHOC; Bogenschutz and Krueger 2013) was proposed for which the higher-order moments needed to construct the PDF are diagnosed instead of prognosed.

The EDMF approach is based on the unification of concepts typically used for the parameterization of boundary layer turbulence (eddy-diffusivity) and moist convection (mass-flux). It was first proposed for dry convective PBLs (Siebesma and Teixeira 2000;
55   Teixeira and Siebesma 2000; Siebesma et al. 2007), and later extended to shallow (e.g., Soares et al. 2004; Neggers 2009; Rio and Hourdin 2008; Suselj et al. 2013, 2019a; Tan et al. 2018), and deep convection (Suselj et al. 2019b; Cohen et al. 2020), with the latter representing fully unified parameterizations. In a nutshell, the EDMF approach combines the eddy-diffusivity (ED) and mass-flux (MF) parameterizations where ED represents the local non-convective mixing and MF represents the nonlocal transport via coherent motions such as updrafts. The stochastic moist multiplume mass-flux approach (Suselj et al. 2013, 2019a,b) consists of a
60   fully-unified EDMF parameterization of PBL turbulence, and dry and moist convection (both shallow and deep) without the usage of trigger functions or cloud-base closures. In its most recent version, the updrafts are coupled to a simple microphysical scheme allowing for precipitating updrafts. A portion of the updrafts' precipitation falls to the surface and the remaining forms downdrafts that may lead to cold pools. Although the precipitating EDMF version is somewhat complex, especially in comparison with its non-precipitating version, it is still fairly computational efficient, making it a strong parameterization candidate for any GCM.
65   Several EDMF versions have been successfully implemented and evaluated in both climate GCMs (Kurowski et al. 2019b; Witte et al. 2022) and operational numerical weather prediction models (e.g., Kohler et al. 2011; Suselj et al. 2014, 2021; Han et al. 2016; Olson et al. 2019).

Despite the recent advances in unified parameterizations, parameterized convection remains one of the largest sources of uncertainty in GCMs. Thus, high-resolution climate modeling (e.g., CRMs) is emerging as a pathway to reduce that uncertainty
70   by explicitly resolving some deep convection. An example of such a model is the Simple Cloud-Resolving E3SM Atmosphere Model (SCREAM) with a target global resolution of 3.25 km (Caldwell et al. 2021), allowing for a more accurate representation of complex mesoscale deep convective dynamics. Nevertheless, small-scale PBL turbulence and shallow convection still need to be parameterized, which is accomplished in SCREAM using the HOC-PDF scheme SHOC for computational efficiency.

Recent studies (Firl and Randall 2015; Fitch 2019) showed that shallow cumulus convection is not properly represented by HOC-PDF schemes due to limitations of the assumed double-Gaussian PDF in representing high skewness and kurtosis of the distributions. Moreover, higher-order moments and cloud statistics appear to only be properly represented when a larger number of Gaussians is used in the joint PDF, which increases its already expensive computational cost. An alternative solution was recently proposed in Witte et al. (2022) where CLUBB is combined with multiple stochastic MF plumes leading to a modified CLUBB+MF parameterization where the plumes represent the extreme tail of the joint distribution which is not represented by CLUBB (see their figure 3). Furthermore, their results showed a large improvement of the higher-order moments for two benchmark shallow cumulus convection cases. Thus, the multiple MF plumes offer a physics-based and cost-effective solution by representing the extreme values of the joint distribution not well captured by the assumed PDF.

Here, our main goal is to improve the representation of shallow cumulus convection in SCREAM by merging SHOC with multiple stochastic MF plumes, thereby creating a unified SHOC+MF parameterization. In our framework, SHOC represents the local mixing and MF the strong nonlocal mixing. The details of the implementation are described in section 2, and the large-eddy simulation (LES) data in section 3. In section 4, we discuss its performance in single-column model (SCM) mode for quasi-steady-state trade-wind maritime shallow cumulus convection, and a land diurnal cycle of shallow convection. Lastly, sensitivity tests to vertical grid-resolution and model time steps are also carried out. Conclusions are presented in section 5.

2 Methodology

We combine a stochastic moist multiplume MF scheme with SHOC (Bogenschutz and Krueger 2013) in SCREAM. The coupling of MF and SHOC has the potential to improve the representation of the mean thermodynamic structure, higher-order moments (e.g., the turbulent fluxes), and cloud macrophysics quantities, by adding the contribution of nonlocal transport during intense convection.

2.1 Host model description

SCREAM emerged as one of the next-generation development efforts of the Energy Exascale Earth System Model (E3SM) project led by the U.S. Department of Energy (DOE) to help guide future energy-sector decisions in light of the current long-term trends due to global warming (Golaz et al. 2019; Caldwell et al. 2021). SCREAM is presently still in development but in its final form aims to represent the next generation of global convection-permitting models (GCPM) by running faster than previous GCPMs due to its performance portability from CPU to GPU machines. To achieve this, the GCM E3SMv1 model serves as a template and is being rewritten from Fortran to C++. SCREAM is based on a nonhydrostatic spectral element dycore and parameterizes turbulence, shallow moist convection, microphysics, radiation, and aerosols (see Caldwell et al. 2021 for a detailed model description). Its target global resolution is 3.25 km.

Here, we use the SCREAM version *dyamond2-try1* still written in Fortran and released in October 2020 (https://github.com/E3SM-Project/scream/releases/tag/dyamond2-try1), with two modifications: (1) multiplume MF scheme implemented in SHOC's codebase, and (2) correction of a bug in the SCM spectral element dynamical core that was producing a strong unphysical temperature cold bias. This bug has been fixed in the current development codebase (https://github.com/E3SM-Project/E3SM/pull/4027).

Our initial assessment of the MF implementation is performed using SCREAM in a SCM framework (Bogenschutz et al. 2020). We are currently migrating the MF component module of the SHOC+MF parameterization to SCREAMv0 (version used in Caldwell et al. 2021), and preliminary results show no significant differences relative to the results presented here.

2.2 EDMF parameterization

In weather and climate models, the prognostic equation of the thermodynamic variables depends on the vertical divergence of the turbulent flux in addition to the advective tendencies and diabatic processes, respectively:

$$\frac{\partial \bar{\phi}}{\partial t} = -\frac{\partial \overline{w'\phi'}}{\partial z} + F_\phi,$$
(1)

where ϕ represents the prognostic horizontally averaged thermodynamic variable, here taken as the liquid water potential temperature and total water mixing ratio, $\phi = \{\theta_l, q_t\}$, w is the vertical velocity, and the primes denote fluctuations with respect to the mean $\bar{\phi}$. In the convective boundary layer, the turbulent flux corresponds to a combination of small-scale and large-scale coherent turbulent structures and can be decomposed as:

$$\overline{w'\phi'} = a_e\overline{w'\phi'}_e + a_e(w_e - \overline{w})(\phi_e - \bar{\phi}) + a_u\overline{w'\phi'}_u + a_u(w_u - \overline{w})(\phi_u - \bar{\phi}),$$
(2)

where the subscripts e and u denote the environment and the strong updrafts, respectively. In the EDMF approach, the following approximations are usually made: 1) the first term is parameterized with the ED approach; 2) the second term is neglected because the environmental and grid-mean values are approximately equal (i.e., $w_e \approx \overline{w}$) following the assumption of small updraft area (i.e., $a_u \ll 1$), and 3) the third term vanishes because the updrafts are assumed horizontally homogeneous and their internal covariances are zero. The fourth term is commonly known as the mass-flux contribution since $M_u \equiv a_u(w_u - \overline{w})$. Thus, (2) can be simplified to:

$$\overline{w'\phi'} = -K_\phi\frac{\partial \bar{\phi}}{\partial z} + M_u(\phi_u - \bar{\phi}),$$
(3)

which encapsulates the eddy-diffusivity/mass-flux (EDMF) approach (e.g., Siebesma et al. 2007; Suselj et al. 2013). Here, the eddy-diffusivity coefficient, K_ϕ, is defined according to SHOC's formulation (Bogenschutz and Krueger 2013), and the MF contribution follows the stochastic moist multiplume MF scheme introduced in Suselj et al 2019a. Thus, the updraft horizontal grid area is partitioned into multiple updrafts, and (3) is rewritten as:

$$\overline{w'\phi'} = -K_\phi\frac{\partial \bar{\phi}}{\partial z} + \sum_{n=1}^{N} M_n(\phi_n - \bar{\phi}),$$
(4)

where $\sum_{n=1}^{N} M_n(\phi_n - \bar{\phi}) = \sum_{n=1}^{N} a_n w_n(\phi_n - \bar{\phi})$, N is the user-selected total number of updrafts (here, $N = 40$ updrafts), a_n is the area fraction of the nth updraft, and w_n and ϕ_n are the vertical velocity and thermodynamic property of the nth updraft. The updraft properties are defined according to the updraft model described below (section 2.3).

It is becoming more common to include downdrafts in EDMF parameterizations (e.g., Wu et al. 2020; Han and Bretherton 2019) mostly due to their relevance to turbulent transport in stratocumulus-topped boundary layers (Chinita et al. 2018; Brient et al. 2019). Despite this, Wu et al. (2020) showed that the inclusion of updrafts is sufficient to represent the vertical thermodynamic structure and turbulent fluxes of non-precipitating stratocumulus, which is in agreement with the findings reported in Matheou and Teixeira (2019) where the authors showed using LES results that the surface buoyancy and wind shear are as important for turbulence production as cloud-top radiative cooling. Combined with a need for computational efficiency, these recent findings led us to neglect downdrafts in our current MF implementation.

2.3 Updraft model

The updraft model closes the multiplume EDMF parameterization, and defines the vertical evolution of an updraft's vertical velocity and thermodynamic properties. Here, we follow the updraft model described in Suselj et al. (2019a). Accordingly, at the surface, we release N independent, steady-state buoyancy-driven updrafts with surface vertical velocities sampled from the right tail of an assumed Gaussian PDF, with values ranging between w_{min} and w_{max}; here defined as $1.5\sigma_w < w_n < 3\sigma_w$, where σ_w is the vertical velocity standard deviation (note that the interval $[1.5\sigma_w, 3\sigma_w]$ corresponds to a total updraft surface fraction area equal to 6.65% in agreement with the sensitivity analysis to the surface updraft area presented in Suselj et al. (2019a)). The tail of the velocity PDF, i.e., the interval $[1.5\sigma_w, 3\sigma_w]$, is discretized into N equidistant bins and the mean vertical velocity value of each bin is associated with a corresponding updraft (N is the total number of updrafts). The surface thermodynamic properties of each updraft are computed by integrating the joint-normal $PDF(\theta_{lu}, q_{tu}, w_u)$ over the updraft's velocity bin (see Suselj et al. 2019b for details on the joint-normal PDF characterization). Here, we use $N = 40$ updrafts. The number of updrafts was chosen based on a sensitivity analysis of SHOC+MF to its value in which SHOC+MF showed weak sensitivity to $N > 30$ updrafts (not shown). Note that a small number of updrafts can produce noisier results due to the lateral entrainment's stochasticity (Suselj et al. 2019a).

The vertical evolution of the nth updraft depends on surface properties and lateral entrainment as follows:

$$\frac{\partial \phi_n}{\partial z} = \varepsilon_n(\phi - \phi_n), \tag{5}$$

where $\phi = (\theta_l, q_t)$, and ε_n is the entrainment rate of the nth updraft. Thus, equation (5) represents the dilution of ϕ_n by lateral entrainment of environmental air ϕ; the environmental air properties are assumed equal to the grid-mean values following Kurowski et al. (2019a). The vertical velocity of the nth updraft is determined by:

$$\frac{\partial w_n^2}{\partial z} = a_w B_n - b_w \varepsilon_n w_n^2, \tag{6}$$

where $a_w = 1$ and $b_w = 1.5$ are constants, and B_n is the updraft's buoyancy given by $B_n = g(\theta_{v,n}/\theta_v - 1)$, where θ_v is the virtual potential temperature. The boundary condition values needed to integrate equations 5 and 6, i.e., the surface thermodynamic properties $(w_n|_s, \theta_{v,n}|_s, q_{t,n}|_s)$, are computed as in Suselj et al. (2019a) and their standard deviation values $(\sigma_w, \sigma_{\theta_v}, \sigma_{q_t})$ follow Suselj et al. (2019b). Note that $\theta_{l,n}|_s$ is defined with respect to $\theta_{v,n}|_s$ as $\theta_{l,n}|_s = \theta_{v,n}|_s/(1 + 0.61 q_{t,n}|_s)$ assuming $\theta_{l,n}|_s \equiv \theta_n|_s$ (subscript s denotes surface). The numerical discretization of equations 5 and 6 follows that described in Suselj et al. (2014).

Lastly, the lateral entrainment of the nth updraft is defined as a stochastic process (Romps and Kuang 2010; Suselj et al. 2019a):

$$\varepsilon_n = \frac{\varepsilon_0}{\Delta z} \mathcal{P}_n\left(\frac{\Delta z}{L_\varepsilon}\right), \tag{7}$$

where ε_0 is the fraction of entrained mass-flux during each entrainment event, here set to $\varepsilon_0 = 0.2$, $\mathcal{P}_n$ is a random number drawn from the Poisson distribution that represents the number of entrainment events for a given average event frequency equal to L_ε, and Δz is the thickness of the respective layer. Note that we evaluate $\mathcal{P}_n$ and ε_n for each updraft independently. Following Suselj et al. (2019b), the entrainment length scale is defined as a function of the depth of the CBL including the cloud layer when present h_{CBL}:

$$L_\varepsilon = a\sqrt{h_{CBL}}, \tag{8}$$

where $a = 1.25$ m$^{1/2}$ is a constant, and h_{CBL} is defined as the model level where the vertical heat flux vanishes ($\overline{w'\theta_l'} \approx 0$). In agreement with previous studies (e.g., Böing et al. 2012; Takahashi et al. 2021), the entrainment length scale L_ε is larger for deeper clouds (i.e., higher h_{CBL}) as these tend to be wider and thus better protected from the environment leading to smaller entrainment

180   rates. Note that diagnosing L_ε as the square-root of h_{CBL} allows for continuous adjustment of ε_n as a function of the CBL state, i.e., the entrainment rate is reduced for deeper CBLs allowing the updrafts to reach higher vertical levels and vice-versa for shallower CBLs, which is particularly important to represent the strong diurnal cycle over land while remaining insensitive to small oscillations of h_{CBL}.

Condensation in each updraft takes place if the updraft water vapor reaches saturation. The MF contribution to the total cloud
185   fraction corresponds to the sum of the area fraction of the updrafts that condense, and the MF contribution to the total cloud water is defined as the area-average of the cloud water of all moist updrafts.

2.4 SHOC

In SCREAM, boundary layer turbulence and moist shallow convection are parameterized by SHOC (Bogenschutz and Krueger 2013). SHOC is considered a simplified assumed PDF-based scheme because the second-order moments needed to construct the

190   PDF are diagnosed instead of prognosed to increase computational efficiency. Accordingly, the turbulent fluxes $\overline{w'\theta_l'}$ and $\overline{w'q_t'}$ are estimated following an eddy-diffusivity approach:

$$\overline{w'\phi'} = -K_\phi \frac{\partial \Phi}{\partial z} \tag{9}$$

where $\phi = \{\theta_l, q_t\}$, and K_ϕ represents the eddy-diffusivity coefficient for heat. It is important to note that SHOC has been updated since Bogenschutz and Krueger (2013) to improve numerical stability and overall performance to better represent the various

195   regimes present in a GCM. For instance, the formulation of the turbulence length scale has been revised, and now follows a continuous formulation instead of two separate definitions for the sub-cloud and cloud layers as documented in Bogenschutz and Krueger (2013). Nevertheless, the SHOC version used in SCREAM exhibits similar scientific performance to the original formulation. For completeness, the turbulence length scale is defined as:

$$L = \frac{1}{l_c}\sqrt{8\left[\frac{1}{\tau\sqrt{e}kz} + \frac{1}{\tau\sqrt{e}L_\infty} + 0.01\delta\frac{N^2}{e}\right]^{-1}}, \tag{10}$$

200   where k is the von Karman constant, e is the turbulent kinetic energy, and $l_c = 0.5$ is the tunable length scale factor. The constant δ is defined as $\delta = 1$ if the Brunt-Vaisala frequency $N^2 > 0$, or $\delta = 0$ if $N^2 \leq 0$ where $N^2 = \frac{g}{\theta_v}\frac{\partial \theta_v}{\partial z}$. The asymptotic value of the length scale L_∞ is defined following Blackadar (1962) as $L_\infty = 0.1 \int_0^\infty \sqrt{e}zdz / \int_0^\infty \sqrt{e}dz$. Lastly, the eddy turnover timescale τ is defined as $\tau = h/w_*$ where h is the boundary layer depth calculated according to Holtslag and Boville (1993), and the convective velocity scale $w_*^3 = 2.5\frac{g}{\theta_v}\int_0^h \overline{w'\theta_v'}dz$. If the boundary layer is stable (i.e., $w_*^3 < 0$), then $\tau = 100$ s.

205   **2.5 Coupling of SHOC and multiplume Mass-Flux parameterizations**

We implement the stochastic multiplume MF scheme in SCREAM by coupling it to SHOC. Thus, the multiplume MF contribution (second term of the right-hand side of equation 11) is added to SHOC's numerical solver for the mean thermodynamic variables, $\phi = (\theta_l, q_t)$, according to the following one-dimensional prognostic equation:

$$\frac{\partial \phi}{\partial t} = -\frac{\partial \overline{w'\phi'}}{\partial z} = -\frac{\partial}{\partial z}\left(\underbrace{-K_\phi \frac{\partial \Phi}{\partial z}}_{SHOC} + \underbrace{\sum_{n=1}^{N} a_n (w_n - \overline{w})(\phi_n - \overline{\phi})}_{MF}\right), \tag{11}$$

where K_ϕ is the eddy diffusivity coefficient, a_n is the area fraction of the nth updraft, w_n and ϕ_n are the vertical velocity and the ϕ value in the nth plume, and the overbar denotes a grid-mean value. The SHOC term (first term of the right-hand side of equation 11) represents the time tendency of ϕ due to the down-gradient diffusion of the mean field and the MF term takes into account the nonlocal transport due to strong convection as discussed in Section 2.2. The prognostic equation 11 is discretized according to the semi-implicit forward-in-time centered-in-space scheme and solved using Richtmyer and Morton (1967) method (see Kurowski et al. (2019) for the discretized form of equation 11). Note that the surface boundary conditions of equation 11 (i.e., the surface fluxes of the thermodynamic variables, $\overline{w'\phi'}_s$) are either calculated by the surface layer parameterization or are prescribed and not modified by the MF component. Results of the coupling of MF and SHOC are denoted as "SHOC+MF" in the next sections.

The shortwave and longwave radiation, and the large-scale cloud microphysics parameterizations are switched off for these experiments—basically because these processes are believed to be of secondary importance for these shallow convection case-studies and as such are also off for the LES experiments. However, cloud fraction and water are calculated at every model level for diagnostic purposes. In SCREAM, the cloud macrophysical properties cloud fraction and liquid water mixing ratio are estimated using the SHOC pdf. Here, the combination of the grid-mean cloud properties is done as a simple weighted sum of the SHOC and MF contributions:

$$CF = CF_{SHOC} + \sum_{n=1}^{N} a_n (q_{l_n} > 0), \tag{12}$$

$$\overline{q_l} = a_e q_{l_{SHOC}} + \sum_{n=1}^{N} a_n q_{l_n}, \tag{13}$$

where CF_{SHOC} and $q_{l_{SHOC}}$ are diagnosed from SHOC's assumed double Gaussian distribution, and a_n and q_{l_n} are the fractional area and condensate loading of the nth updraft. Note that in practice, although the algorithm also imposes $CF \leq 1$, this value is not reached in these simulations because of the low values typical of these shallow convection case-studies. These low cloud values, the overall cloud vertical structure of these shallow convection regimes, and the fact that the radiation parameterization is off, are the key reasons for not using more complex cloud overlap algorithms in these estimates.

2.6 Single-column model simulations

The ability of the unified SHOC+MF parameterization to represent shallow cumulus boundary layers has been investigated by simulating benchmark cases including the shallow cumulus Barbados Oceanographic and Meteorological Experiment BOMEX (Siebesma et al. 2003)—quasi-steady-state warm maritime shallow convection over the Atlantic Ocean in June 1969, and the Atmospheric Radiation Measurement (ARM) shallow cumulus case (Brown et al. 2002)—diurnal cycle of warm shallow convection over land at the Southern Great Plains site of the ARM program on 21 June 1997. The two cases were simulated using SCREAM in a SCM framework in which we used the intensive observation period (IOP) forcing files available in the E3SM SCM library (Bogenschutz et al. 2020) with prescribed horizontal large-scale forcing and surface turbulent fluxes. It is worth noting that we modified the ARM case forcing file to run the model with a 30-minute time step (i.e., the ARM forcing file available in the E3SM SCM library contains values at every 20 minutes). Also, the SCM reads the wind information from the forcing file at every host model time step, however for the ARM case, the large-scale advective tendencies of the winds were not available when the case was setup (Brown et al. 2002), and consequently, the time-varying u profiles in the forcing file were set equal to the initial profiles which are constant with height. Resetting the u profile to the initial vertically constant profile at every host model time step interferes with the development of the TKE field through the shear production term. To circumvent this issue, we replaced the

u profiles in the forcing file with the u profiles from our LES reference data; the meridional wind component v is zero in the ARM case. Note that this is specific to the SCM used here and to the ARM case as the large-scale advective tendencies of the winds were not available when the ARM case was setup (Brown et al. 2002).

We kept the default host model setup but deactivated the deep convection, large-scale microphysics and radiation schemes to allow for a more straightforward comparison with our LES reference data. The dynamic and physics time steps are equal to 30 minutes and 5 minutes, respectively. For our initial implementation and performance evaluation, we used a 72-layer vertical grid (L72) with 21 levels resolving the bottom 3 km. In section 4.4, we conduct tests to quantify sensitivity to the vertical grid resolution and to the time step using BOMEX. Thus, for the vertical grid resolution, we assess the sensitivity of the results using L72 and a relatively-finer 128-layer vertical grid (L128) with twice as many grid-cells resolving the bottom 3 km (40 grid-cells). For the time step sensitivity, we compare the results using the L128 and dynamics and physics time steps equal to 30 minutes and 5 minutes (300 seconds), respectively, with dynamics and physics time steps both equal to 75 seconds which resembles the configuration used in Caldwell et al. (2021) for the first global results of SCREAM in convection-permitting mode ($\Delta x = 3.25$ km). Lastly, we used a total of $N = 40$ updrafts.

3 Large-eddy simulation model

We evaluate our SHOC+MF parameterization by comparing it to LES output of the same simulated cases. This LES reference data are acquired with the LES model of Matheou and Chung (2014). Table 1 summarizes the LES runs and their configurations. The computational domain is doubly periodic in the horizontal directions and all grids are uniform and isotropic ($\Delta x = \Delta y = \Delta z$). The simulations have different domain sizes in the vertical adjusted to their respective boundary layer depths. A Rayleigh damping layer is imposed near the domain top to mitigate gravity wave reflection and the surface turbulent fluxes are prescribed as in the SCREAM SCM. The momentum and scalar advection terms are discretized according to the sixth-order fully conservative centered scheme of Morinishi et al. (1998) adapted for the anelastic approximation (Matheou et al. 2016). The subgrid-scale (SGS) turbulence is represented by the buoyancy-adjusted stretched-vortex SGS model (Chung and Matheou 2014). Precipitation is neglected in the LES model according to the case descriptions (Brown et al. 2002; Siebesma et al. 2003) and all water condensate is assumed suspended using an "all or nothing" saturation adjustment scheme based on the local grid-mean state. The simulations are carried out in the frame of reference of the domain-mean horizontal wind to reduce numerical errors (Lamaakel and Matheou 2021). The LES model has been successfully used in previous studies spanning several meteorological conditions (Chung et al. 2012; Matheou and Chung 2014; Matheou 2018; Matheou and Teixeira 2019; Couvreux et al. 2020; Chinita et al. 2022a,b).

Table 1 Summary of the cases simulated. The details of each case setup are described in the references (second column). Here, $L_{x,y}$ and L_z are the horizontal and vertical domain lengths, $N_{x,y}$ and N_z are the number of horizontal and vertical grid points, and Δx is the grid spacing.

Case	Reference	$L_{x,y}$ (km)	L_z (km)	$N_{x,y}$	N_z	Δx
Maritime shallow convection	Siebesma et al (2003)	20.48	3.0	1024	150	20
Continental shallow convection	Brown et al. (2002)	20.48	4.4	1024	220	20

4 Results

We compare the results of SHOC and SHOC+MF against the LES reference data for the benchmark cases listed in section 2.5. Note that in SHOC+MF, we reduced SHOC's turbulence mixing length scale relative to SHOC alone, to prevent excessive mixing. This was done by increasing the tunable length scale factor l_c from 0.5 to 1 in equation 10. Thus, $l_c = 0.5$ in the SHOC experiments, and $l_c = 1$ in the SHOC+MF experiments. All other model and parameterization configurations were kept the same for all simulations shown here. Lastly, for the simulations of SHOC alone, we used the same tunable constants from the global high-resolution simulation presented in Caldwell et al. (2021).

4.1 Trade-wind maritime shallow cumulus

Figure 1 shows results for BOMEX averaged over simulated hours 4 to 6. The thermodynamics profiles are generally similar but with some noticeable differences: SHOC is colder above cloud base and warmer near the cloud top relative to the LES (Figure 1a), and it is moister above cloud base and drier near the cloud top (Figure 1b). This is because SHOC mixes excessively up to ~ 1 km and does not reproduce a shallow cumulus layer (Figure 1d and e). Consequently, moisture does not reach the levels where the cloud top should be located and instead, it gets trapped between 0.5 and 1 km. In contrast, the turbulent transport of SHOC+MF is very similar to the LES leading to comparable thermodynamic profiles, except near the cloud top (~ 1.5 km) where SHOC+MF mixes slightly less leading to a drier (warmer) layer relative to the LES. The partitioning of turbulent transport between local and nonlocal mixing in SHOC+MF is similar to previous EDMF studies (e.g., Suselj et al. 2013; Kurowski et al. 2019), i.e., the local mixing dominates in the subcloud layer and MF takes over in the cloud layer.

Because of the excessive humidity between 0.5 and 1 km in SHOC, the cloud fraction and liquid water mixing ratio are overestimated relative to the LES (Figure 1c and f). On the other hand, SHOC+MF captures the profiles of both cloud fraction and cloud liquid water content fairly well due to the adequate vertical distribution of the thermodynamic quantities. Note that the cloud fraction and liquid water content of SHOC+MF shown in Figure 1 are calculated as the sum of SHOC and MF contributions.

A key aspect in simulating shallow cumulus with an MF-type parameterization like SHOC+MF is the accurate representation of the moist updraft properties (i.e., updraft area, vertical velocity, and the excess of moist conserved variables). Figure 2 shows the moist updraft properties of the mass-flux of SHOC+MF and the respective LES values based on cloud ($q_l > 1 \times 10^{-5}$ kg kg^{-1}) and cloud core ($q_l > 1 \times 10^{-5}$ kg kg^{-1}, $w > 0$, $\theta_v > \langle \theta_v \rangle$ where the angle brackets denote the instantaneous horizontal average of the LES domain) samplings (Siebesma and Cuijpers 1995). Since the SHOC+MF turbulent transport is controlled mostly by MF in the cloud layer (dashed profiles in Figure 1d and e), the moist updraft properties should lie close to the LES cloud and cloud core values (Couvreux et al. 2010; Suselj et al. 2013; Kurowski et al. 2019b). The SHOC+MF updraft area agrees reasonably well with the LES values, especially when considering the relatively coarse vertical grid used here, resulting in just two grid levels to resolve the sharp increase near the cloud base. The vertical velocity and the excess of updraft moist conserved variables relative to the grid-mean values of SHOC+MF are close to the LES profiles, except in the middle of the cloud layer (~1 km) where the θ_{lu} and q_{tu} excesses are underestimated. This is due to the slight overestimation of the SHOC+MF grid-mean q_t (Figure 1b) relative to the LES. Nevertheless, the SHOC+MF moist updraft properties agree well with the LES, which confirms the suitable behavior of our MF scheme. Note that the "updraft" (second Gaussian) moist properties of the SHOC's PDF are not shown because they are quite small (e.g., maximum $w_u \approx 0.3$ m/s) and vanish around 800 m in agreement with Figure 1d-e where the MF contribution makes up the total turbulent fluxes.

4.2 Continental shallow cumulus

The ARM shallow cumulus case represents a diurnal cycle of warm convection over land at the Southern Great Plains site of the ARM program on 21 June 1997 (Brown et al. 2002). The case starts with a morning transition at 11:30 UTC (5:30 LST—local standard time) from a stable boundary layer (negative surface heat flux until 1.5 simulated hours) to a fully developed CBL with a top close to 2.5 km at around 21:00 UTC (15:00 LST). The case represents a typical buoyancy-driven shallow cumulus case where convection is primarily forced by the surface sensible and latent heat fluxes. The nonstationary conditions of the ARM shallow cumulus case make it more challenging to properly simulate than the quasi-steady-state BOMEX case.

Figure 3 shows that the diurnal evolution of hourly mean thermodynamic profiles is well represented by SHOC+MF, whereas SHOC produces a warm (dry) bias in the subcloud layer and a cold (moist) bias near the cloud top. To illustrate the magnitude and temporal evolution of these biases, panels a and b of Figure 4 show the temperature and moisture differences relative to the LES fields, and by the end of the simulation, the temperature (moisture) bias exceeds 0.5 K (1 g kg^{-1}) in the subcloud layer and 1.5 K (4 g kg^{-1}) near the cloud top. On the other hand, SHOC+MF is able to reproduce the diurnal evolution of the PBL and cloud layer remarkably well for both thermodynamic quantities. The largest bias is located near the surface for the total water mixing ratio with maximum deviations from LES around +0.5 g kg^{-1} (Figure 4d).

Figure 5 shows the diurnal evolution of hourly mean profiles of the turbulent fluxes of liquid water potential temperature (top row) and total water mixing ratio (bottom row). In agreement with the vertical distribution of the thermodynamic quantities, SHOC+MF represents fairly well both turbulent transports, whereas SHOC produces excessive turbulent mixing and consequently places the cloud top near 3 km at 20:30 UTC—about 1 km deeper than the LES. Figure 6 shows the differences between the temperature and moisture turbulent fluxes of SHOC and SHOC+MF relative to the LES. Both temperature and moisture panels (a-b) confirm SHOC's excessive mixing and cloud layer deepening, and also reveal oscillations, particularly on the $\overline{w'q_t'}$ field after hour 5. These oscillations may be due to the eddy turnover timescale τ used in the calculation of SHOC's turbulence mixing length scale (equation 10) in this SCREAM version since these are not present when a constant timescale is used (e.g., $\tau = 400$ seconds; not shown). However, SHOC+MF is able to reproduce the turbulent fluxes without these oscillations (Figure 6 c-d) while using the dynamic timescale, matching the LES reasonably well, except for the last 4 hours of simulation where $\overline{w'q_t'}$ decreases slower (faster) than the LES in the upper-half (lower-half) of the boundary layer (Figure 5h).

Note that the turbulent transport partition between local and nonlocal mixing in SHOC+MF is similar to BOMEX when the cloud layer forms (from simulated hour 5 to hour 12), i.e., the transport is mostly controlled by the local mixing in the subcloud layer whereas MF dominates in the cloud layer (e.g., dashed red profiles in Figure 5c and g). Before cloud formation, the local mixing contribution to the turbulent transport is larger and the MF contribution is only significant near the surface. A similar behavior was observed for a dry convection case (case 1 of Siebesma et al. 2007—not shown), where SHOC properly represented the turbulent transport including the PBL growth, but developed a warm bias near the surface—this is a typical pattern of ED-type schemes without MF (e.g., Teixeira and Cheinet 2004; Siebesma et al. 2007; Witek et al. 2011). The inclusion of MF partially reduced this warm bias by slightly enhancing the turbulent mixing near the surface whilst adjusting its contribution to negligible values away from the surface.

Figure 7 shows the temporal evolution of the cloud fraction. The LES cloud fraction field is smoother than SHOC and SHOC+MF due to the LES higher temporal resolution ($\Delta t = 1$ minute vs 30 minutes). Nevertheless, SHOC+MF cloud cover (Figure 7c) roughly follows the LES, except between hours 10 and 12 because of its excessive turbulent flux in the cloud layer (Figure 5h) resulting in significantly higher cloud fraction values. The cloud fraction values of SHOC surpass those from LES because of the

excessive moisture content in the cloud layer (Figure 4b) and its onset happens about 1 hour earlier than in the LES. Conversely, SHOC+MF captures the cloud layer evolution reasonably well due to a better representation of the heat and moisture turbulent transports (Figure 5 and Figure 6c-d).

4.3 Sensitivity to vertical grid-resolution and time step

The sensitivity of SHOC and SHOC+MF results to the vertical grid-resolution and time step is explored here using the BOMEX case. Results are similar for the ARM case and thus are omitted. We compare the results of BOMEX discussed in section 4.1 using the default vertical grid (72 vertical levels; L72) and a 128-layer vertical grid (L128). This vertical resolution increase translates to about twice as many grid cells within the CBL (including the cloud layer). All other aspects of the model configuration were held unchanged. Lastly, we use the L128 grid to explore the sensitivity of the model to the time step comparing the default 30-minute time step to a 75-second time step. The vertical grid and the time step used in SCREAM's global simulations will likely be close to L128 and $\Delta t = 75$ seconds (Caldwell et al. 2021), thus the importance of exploring the sensitivity of SHOC+MF to both configurations.

Figure 8 shows the sensitivity of the temporally averaged vertical profiles of the thermodynamic and cloud macrophysics variables, and turbulent fluxes with respect to the vertical grids. The results of SHOC+MF demonstrate low sensitivity to the grid resolution but still a slight improvement when using L128, e.g., unsurprisingly, the sharp increase in cloud fraction near the cloud base is better resolved with L128 (Figure 8c although not clearly visible). On the other hand, the results of SHOC show a strong sensitivity to the grid resolution, specifically both heat and moisture turbulent fluxes roughly double in magnitude in the cloud layer (Figure 8d–e). On a positive note, this increase in turbulent transport warms up the cloud layer relative to the results using L72, which improves the cloud fraction.

The sensitivity with respect to the time step is shown in Figure 9. The results of SHOC+MF also show low sensitivity to the time step, while SHOC seems to be slightly sensitive to it. Overall, the results of SHOC+MF do not depend on the vertical grid resolution and on the time step. Thus, further tuning does not seem to be necessary for shallow convection when using a different vertical grid or time step.

5   Conclusions

This study documents the implementation of the stochastic multiplume mass-flux (MF) parameterization (Suselj et al. 2013, 2019b,a) in the Simple Cloud-Resolving E3SM Atmosphere Model (SCREAM) by coupling it to the Simplified-Higher-Order Closure (SHOC) turbulence and cloud macrophysics scheme. The MF contribution to the total turbulent transport is added to SHOC's numerical solver for the moist conserved thermodynamic variables.

SHOC is a unified assumed PDF-based scheme that represents both boundary layer turbulence and cloud macrophysics, and while it satisfactorily represents dry convection and stratocumulus layers, it struggles to adequately represent shallow cumulus convection (Firl and Randall 2015; Fitch 2019). Following a recent study that showed promising results in solving this issue by combining an MF parameterization with the assumed PDF scheme CLUBB (Witte et al. 2022), we coupled MF to SHOC to improve the representation of shallow cumulus convection in SCREAM.

Our new scheme (SHOC+MF) was evaluated in a single-column simulation (SCM) framework against LES reference data for two shallow cumulus convection cases: BOMEX—quasi-steady warm maritime shallow convection, and ARM—diurnal cycle of warm

shallow convection over land. We also compared the SHOC+MF results with standard SHOC. In general, SHOC+MF represents
well the mean and flux profiles of moist conserved thermodynamic variables (liquid water potential temperature θ_l, and total water
mixing ratio q_t), as well as the cloud macrophysics properties (cloud fraction and cloud water mixing ratio q_c) for shallow cumulus
boundary layers. This represents an improvement versus SHOC alone, since for BOMEX, SHOC does not reproduce a shallow
cumulus layer but rather simulates a structure similar to a stratocumulus boundary layer, and for ARM, SHOC mixes excessively
up to 3 km producing a cloud layer too deep, and also overestimates the cloud macrophysical properties.

We performed a sensitivity analysis to the vertical grid resolution, and dynamic and physics time step for SHOC and SHOC+MF.
While SHOC seems to be sensitive to both grid resolution and time step, SHOC+MF showed weak sensitivity to both. Thus,
SHOC+MF appears to be robust to changes in the vertical resolution and time step, suggesting there is no need for additional
parameter optimization.

In summary, the results of SHOC+MF in SCREAM demonstrate good performance by improving the representation of shallow
cumulus convection. Furthermore, the SHOC+MF configuration introduced here is robust enough to properly represent two
different shallow cumulus convection cases (i.e., quasi-stationary and non-stationary) regardless of the vertical grid resolution and
time step used. Based on these encouraging results, we are currently expanding the evaluation of SHOC+MF to both stratocumulus
and deep convection regimes, and to global simulations.

Code and data availability

In this study, we used the E3SM model (https://doi.org/10.11578/E3SM/dc.20210927.1), specifically the E3SM SCREAM version
dyamond2-try1 released in October 2020 (https://github.com/E3SM-Project/scream/releases/tag/dyamond2-try1). The modified
code shoc.F90 and shoc_intr.F90, the mass_flux.F90, and the scripts and respective IOP files used to generate the present SCM
simulations are archived at https://doi.org/10.5281/zenodo.7011628. The SCM and LES output data are archived at
https://doi.org/10.5281/zenodo.7011652.

Author contributions

Maria J. Chinita: conceptualization; methodology; formal analysis; visualization. **Mikael Witte:** conceptualization;
methodology. **Marcin J. Kurowski**: conceptualization; methodology. **J. Teixeira**: conceptualization; methodology; supervision.
Kay Suselj: conceptualization; methodology. **Georgios Matheou**: provided the large-eddy simulation output data. **Peter
Bogenschutz**: provided crucial SCREAM code assistance. All authors contributed to interpreting the results, writing and reviewing
the manuscript.

Competing interests

The authors declare that they have no competing interests.

Acknowledgements

Part of this research was carried out at the Jet Propulsion Laboratory, California Institute of Technology, under a contract with the
National Aeronautics and Space Administration (80NM0018D0004). We gratefully acknowledge the support of the U.S.
Department of Energy, Office of Biological and Environmental Research, Earth System Modeling (DE-SC0019242). This research
used resources from the National Energy Research Scientific Computing Center (NERSC), a U.S. Department of Energy Office of
Science User Facility located at Lawrence Berkeley National Laboratory, operated under Contract No. DE-AC02-05CH11231.

References

Beljaars, A., and Coauthors, 2018: The Numerics of Physical Parametrization in the ECMWF Model. *Front. Earth Sci.*, **6**, 1–18, https://doi.org/10.3389/feart.2018.00137.

Betts, A. K., 1973: Non-precipitating cumulus convection and its parameterization. *Q. J. R. Meteorol. Soc.*, **99**, 178–196, https://doi.org/10.1002/qj.49709941915.

Blackadar, A. K., 1962: The vertical distribution of wind and turbulent exchange in a neutral atmosphere. *J. Geophys. Res.*, **67**, 3095–3102.

Bogenschutz, P. A., and S. K. Krueger, 2013: A simplified PDF parameterization of subgrid-scale clouds and turbulence for cloud-resolving models. *J. Adv. Model. Earth Syst.*, **5**, 195–211, https://doi.org/10.1002/jame.20018.

——, S. Tang, P. M. Caldwell, S. Xie, W. Lin, and Y. S. Chen, 2020: The E3SM version 1 single-column model. *Geosci. Model Dev.*, **13**, 4443–4458, https://doi.org/10.5194/gmd-13-4443-2020.

Böing, S. J., H. J. J. Jonker, A. P. Siebesma, and W. W. Grabowski, 2012: Influence of the subcloud layer on the development of a deep convective ensemble. *J. Atmos. Sci.*, **69**, 2682–2698, https://doi.org/10.1175/JAS-D-11-0317.1.

Brient, F., F. Couvreux, N. Villefranque, C. Rio, and R. Honnert, 2019: Object-Oriented Identification of Coherent Structures in Large Eddy Simulations: Importance of Downdrafts in Stratocumulus. *Geophys. Res. Lett.*, **46**, 2854–2864, https://doi.org/10.1029/2018GL081499.

Brown, A. R., and Coauthors, 2002: Large-eddy simulation of the diurnal cycle of shallow cumulus convection over land. *Q. J. R. Meteorol. Soc.*, **128**, 1075–1093, https://doi.org/10.1256/003590002320373210.

Caldwell, P. M., and Coauthors, 2021: Convection-Permitting Simulations With the E3SM Global Atmosphere Model. *J. Adv. Model. Earth Syst.*, **13**, 47, https://doi.org/10.1029/2021MS002544.

Cheng, A., and K. M. Xu, 2006: Simulation of shallow cumuli and their transition to deep convective clouds by cloud-resolving models with different third-order turbulence closures. *Q. J. R. Meteorol. Soc.*, **132**, 359–382, https://doi.org/10.1256/qj.05.29.

——, and ——, 2008: Simulation of boundary-layer cumulus and stratocumulus clouds using a cloud-resolving model with low- and third-order turbulence closures. *J. Meteorol. Soc. Japan*, **86A**, 67–86, https://doi.org/10.2151/jmsj.86A.67.

Chinita, M. J., G. Matheou, and J. Teixeira, 2018: A joint probability density-based decomposition of turbulence in the atmospheric boundary layer. *Mon. Weather Rev.*, **146**, https://doi.org/10.1175/MWR-D-17-0166.1.

Chinita, M. J., G. Matheou, and P. M. A. Miranda, 2022a: Large-eddy simulation of very stable boundary layers. Part I: Modeling methodology. *Q. J. R. Meteorol. Soc.*, 1–19, https://doi.org/https://doi.org/10.1002/qj.4279.

——, G. Matheou, and P. M. A. Miranda, 2022b: Large-eddy simulation of very stable boundary layers. Part II: Length scales and anisotropy in stratified atmospheric turbulence. *Q. J. R. Meteorol. Soc.*, 1–16, https://doi.org/https://doi.org/10.1002/qj.4280.

Chung, D., and G. Matheou, 2014: Large-eddy simulation of stratified turbulence. Part I: A vortex-based subgrid-scale model. *J. Atmos. Sci.*, **71**, 1863–1879, https://doi.org/10.1175/JAS-D-13-0126.1.

Chung, D., G. Matheou, and J. Teixeira, 2012: Steady-state large-eddy simulations to study the stratocumulus to shallow cumulus cloud transition. *J. Atmos. Sci.*, **69**, 3264–3276, https://doi.org/10.1175/JAS-D-11-0256.1.

Cohen, Y., I. Lopez-Gomez, A. Jaruga, J. He, C. M. Kaul, and T. Schneider, 2020: Unified Entrainment and Detrainment Closures for Extended Eddy-Diffusivity Mass-Flux Schemes. *J. Adv. Model. Earth Syst.*, **12**, e2020MS002162, https://doi.org/https://doi.org/10.1029/2020MS002162.

Couvreux, F., F. Hourdin, and C. Rio, 2010: Resolved versus parametrized boundary-layer plumes. Part I: A parametrization-

oriented conditional sampling in large-eddy simulations. *Boundary-Layer Meteorol.*, **134**, 441–458, https://doi.org/10.1007/s10546-009-9456-5.

Couvreux, F., and Coauthors, 2020: Intercomparison of Large-Eddy Simulations of the Antarctic Boundary Layer for Very Stable Stratification. *Boundary-Layer Meteorol.*, **176**, 369–400, https://doi.org/10.1007/s10546-020-00539-4.

500 Deardorff, J. W., 1966: The Counter-Gradient Heat Flux in the Lower Atmosphere and in the Laboratory. *J. Atmos. Sci.*, **23**, 503–506, https://doi.org/10.1175/1520-0469(1966)023<0503:tcghfi>2.0.co;2.

Firl, G. J., and D. A. Randall, 2015: Fitting and analyzing les using multiple trivariate Gaussians. *J. Atmos. Sci.*, **72**, 1094–1116, https://doi.org/10.1175/JAS-D-14-0192.1.

Fitch, A. C., 2019: An improved double-Gaussian closure for the subgrid vertical velocity probability distribution function. *J.*
505 *Atmos. Sci.*, **76**, 285–304, https://doi.org/10.1175/JAS-D-18-0149.1.

Golaz, J. C., V. E. Larson, and W. R. Cotton, 2002: A PDF-based model for boundary layer clouds. Part I: Method and model description. *J. Atmos. Sci.*, **59**, 3540–3551, https://doi.org/10.1175/1520-0469(2002)059<3540:APBMFB>2.0.CO;2.

——, and Coauthors, 2019: The DOE E3SM Coupled Model Version 1: Overview and Evaluation at Standard Resolution. *J. Adv. Model. Earth Syst.*, **11**, 2089–2129, https://doi.org/10.1029/2018MS001603.

510 Han, J., and H. L. Pan, 2011: Revision of convection and vertical diffusion schemes in the NCEP Global Forecast System. *Weather Forecast.*, **26**, 520–533, https://doi.org/10.1175/WAF-D-10-05038.1.

——, and C. S. Bretherton, 2019: TKE-based moist eddy-diffusivity mass-flux (EDMF) parameterization for vertical turbulent mixing. *Weather Forecast.*, **34**, 869–886, https://doi.org/10.1175/WAF-D-18-0146.1.

——, M. L. Witek, J. Teixeira, R. Sun, H. L. Pan, J. K. Fletcher, and C. S. Bretherton, 2016: Implementation in the NCEP GFS
515 of a hybrid eddy-diffusivity mass-flux (EDMF) boundary layer parameterization with dissipative heating and modified stable boundary layer mixing. *Weather Forecast.*, **31**, 341–352, https://doi.org/10.1175/WAF-D-15-0053.1.

Holtslag, A. A. M., and C.-H. Moeng, 1991: Eddy diffusivity and countergradient transport in the convective atmospheric boundary layer. *J. Atmos. Sci.*, **48**, 1690–1698, https://doi.org/10.1175/1520-0469(1991)048<1690:EDACTI>2.0.CO;2.

——, and B. A. Boville, 1993: Local versus nonlocal boundary-layer diffusion in a global climate model. *J. Clim.*, **6**, 1825–
520 1842, https://doi.org/10.1175/1520-0442(1993)006<1825:LVNBLD>2.0.CO;2.

Kohler, M., M. Ahlgrimm, and A. Beljaars, 2011: Unified treatment of dry convective and stratocumulus-topped boundary layers in the ECMWF model. *Q. J. R. Meteorol. Soc.*, **137**, 43–57, https://doi.org/10.1002/qj.713.

Kurowski, M. J., K. Suselj, and W. W. Grabowski, 2019a: Is Shallow Convection Sensitive to Environmental Heterogeneities? *Geophys. Res. Lett.*, **46**, 1785–1793, https://doi.org/10.1029/2018GL080847.

525 ——, H. T. Thrastarson, K. Suselj, and J. Teixeira, 2019b: Towards unifying the planetary boundary layer and shallow convection in CAM5 with the eddy-diffusivity/mass-flux approach. *Atmosphere*, **10**, 1–20, https://doi.org/10.3390/atmos10090484.

Lamaakel, O., and G. Matheou, 2021: Galilean invariance of shallow cumulus convection large-eddy simulations. *J. Comput. Phys.*, **427**, 110012, https://doi.org/https://doi.org/10.1016/j.jcp.2020.110012.

530 Matheou, G., 2018: Turbulence Structure in a Stratocumulus Cloud. *Atmos.* , **9**, https://doi.org/10.3390/atmos9100392.

——, and D. Chung, 2014: Large-eddy simulation of stratified turbulence. Part II: Application of the stretched-vortex model to the atmospheric boundary layer. *J. Atmos. Sci.*, **71**, 4439–4460, https://doi.org/10.1175/JAS-D-13-0306.1.

——, and J. Teixeira, 2019: Sensitivity to physical and numerical aspects of large-eddy simulation of stratocumulus. *Mon. Weather Rev.*, **147**, 2621–2639, https://doi.org/10.1175/MWR-D-18-0294.1.

535 Matheou, G., D. Chung, and J. Teixeira, 2016: On the synergy between numerics and subgrid scale modeling in LES of stratified

flows: Grid convergence of a stratocumulus-topped boundary layer. *International Symposium on Stratified Flows*.

Morinishi, Y., T. S. Lund, O. V Vasilyev, and P. Moin, 1998: Fully Conservative Higher Order Finite Difference Schemes for Incompressible Flow. *J. Comput. Phys.*, **143**, 90–124, https://doi.org/https://doi.org/10.1006/jcph.1998.5962.

Neggers, R. A. J., 2009: A dual mass flux framework for boundary layer convection. Part II: Clouds. *J. Atmos. Sci.*, **66**, 1489–1506, https://doi.org/10.1175/2008JAS2636.1.

Olson, J. B., J. S. Kenyon, W. A. Angevine, J. M. Brown, M. Pagowski, and K. Sušelj, 2019: A Description of the MYNN-EDMF Scheme and the Coupling to Other Components in WRF–ARW. https://doi.org/https://doi.org/10.25923/n9wm-be49.

Richtmyer, R., and K. Morton, 1967: *Difference methods for initial value problems.* Interscience Publishers, 405 pp.

Rio, C., and F. Hourdin, 2008: A thermal plume model for the convective boundary layer: Representation of cumulus clouds. *J. Atmos. Sci.*, **65**, 407–425, https://doi.org/10.1175/2007JAS2256.1.

Romps, D. M., and Z. Kuang, 2010: Nature versus nurture in shallow convection. *J. Atmos. Sci.*, **67**, 1655–1666, https://doi.org/10.1175/2009JAS3307.1.

Schneider, T., J. Teixeira, C. S. Bretherton, F. Brient, K. G. Pressel, C. Schär, and A. P. Siebesma, 2017: Climate goals and computing the future of clouds. *Nat. Clim. Chang.*, **7**, 3–5, https://doi.org/10.1038/nclimate3190.

Sherwood, S. C., S. Bony, and J. L. Dufresne, 2014: Spread in model climate sensitivity traced to atmospheric convective mixing. *Nature*, **505**, 37–42, https://doi.org/10.1038/nature12829.

Siebesma, A., and Coauthors, 2003: A large eddy simulation intercomparison study of shallow cumulus convection. *J. Atmos. Sci.*, **60**, 1201–1219, https://doi.org/10.1175/1520-0469(2003)60<1201:ALESIS>2.0.CO;2.

Siebesma, A. P., and J. W. M. Cuijpers, 1995: Evaluation of parametric assumptions for shallow cumulus convection. *J. Atmos. Sci.*, **52**, 650–666, https://doi.org/10.1175/1520-0469(1995)052<0650:EOPAFS>2.0.CO;2.

Siebesma, A. P., P. M. M. Soares, and J. Teixeira, 2007: A combined eddy-diffusivity mass-flux approach for the convective boundary layer. *J. Atmos. Sci.*, **64**, 1230–1248, https://doi.org/10.1175/JAS3888.1.

Siebesma, P., and J. Teixeira, 2000: An advection-diffusion scheme for the convective boundary layer: Description and 1D-results. *14th Symp. on Boundary Layer Turbulence*, Aspen, CO, Amer. Meteor. Soc., 133–136.

Soares, P. M. M., P. M. A. Miranda, A. P. Siebesma, and J. Teixeira, 2004: An eddy-diffusivity/mass-flux parametrization for dry and shallow cumulus convection. *Q. J. R. Meteorol. Soc.*, **130 C**, 3365–3383, https://doi.org/10.1256/qj.03.223.

Stevens, B., 2000: Quasi-steady analysis of a PBL model with an Eddy-diffusivity profile and nonlocal fluxes. *Mon. Weather Rev.*, **128**, 824–836, https://doi.org/10.1175/1520-0493(2000)128<0824:QSAOAP>2.0.CO;2.

Suselj, K., J. Teixeira, and D. Chung, 2013: A unified model for moist convective boundary layers based on a stochastic eddy-diffusivity/mass-flux parameterization. *J. Atmos. Sci.*, **70**, 1929–1953, https://doi.org/10.1175/JAS-D-12-0106.1.

——, T. F. Hogan, and J. Teixeira, 2014: Implementation of a stochastic eddy-diffusivity/mass-flux parameterization into the Navy Global environmental model. *Weather Forecast.*, **29**, 1374–1390, https://doi.org/10.1175/WAF-D-14-00043.1.

——, M. J. Kurowski, and J. Teixeira, 2019a: On the factors controlling the development of shallow convection in eddy-diffusivity/mass-flux models. *J. Atmos. Sci.*, **76**, 433–456, https://doi.org/10.1175/JAS-D-18-0121.1.

——, ——, and J. Teixeira, 2019b: A unified eddy-diffusivity/mass-flux approach for modeling atmospheric convection. *J. Atmos. Sci.*, **76**, 2505–2537, https://doi.org/10.1175/JAS-D-18-0239.1.

——, J. Teixeira, M. J. Kurowski, and A. Molod, 2021: Improving the representation of subtropical boundary layer clouds in the NASA GEOS model with the eddy-diffusivity/mass-flux parameterization. *Mon. Weather Rev.*, **149**, 793–809, https://doi.org/10.1175/MWR-D-20-0183.1.

Takahashi, H., Z. J. Luo, and G. Stephens, 2021: Revisiting the Entrainment Relationship of Convective Plumes: A Perspective From Global Observations. *Geophys. Res. Lett.*, **48**, 1–7, https://doi.org/10.1029/2020GL092349.

Tan, Z., C. M. Kaul, K. G. Pressel, Y. Cohen, T. Schneider, and J. Teixeira, 2018: An Extended Eddy-Diffusivity Mass-Flux Scheme for Unified Representation of Subgrid-Scale Turbulence and Convection. *J. Adv. Model. Earth Syst.*, **10**, 770–800, https://doi.org/https://doi.org/10.1002/2017MS001162.

Teixeira, J., and P. Siebesma, 2000: A mass flux/K-diffusion approach to the parameterization of the convective boundary layer: Global model results. *14th Symp. on Boundary Layers Turbulence*, Aspen, CO, Amer. Meteor. Soc, 231–234.

——, and S. Cheinet, 2004: A simple mixing length formulation for the eddy-diffusivity parameterization of dry convection. *Boundary-Layer Meteorol.*, **110**, 435–453, https://doi.org/10.1023/B:BOUN.0000007230.96303.0d.

Teixeira, J., J. P. Ferreira, P. M. A. Miranda, T. Haack, J. Doyle, A. P. Siebsema, and R. Salgado, 2004: A new mixing-length formulation for the parameterization of dry convection: Implementation and evaluation in mesoscale model. *Mon. Weather Rev.*, **132**, 2698–2707, https://doi.org/10.1175/MWR2808.1.

——, and Coauthors, 2008: Parameterization of the atmospheric boundary layer: A view from just above the inversion. *Bull. Am. Meteorol. Soc.*, **89**, 453–458, https://doi.org/10.1175/BAMS-89-4-453.

Tiedtke, M., 1989: A Comprehensive Mass Flux Scheme for Cumulus Parameterization in Large-Scale Models. *Mon. Weather Rev.*, **117**, 1779–1800.

Witek, M. L., J. Teixeira, and G. Matheou, 2011: An Integrated TKE-based eddy diffusivity/mass flux boundary layer closure for the dry convective boundary layer. *J. Atmos. Sci.*, **68**, 1526–1540, https://doi.org/10.1175/2011JAS3548.1.

Witte, M. K., and Coauthors, 2022: Augmenting the double-Gaussian representation of atmospheric turbulence and convection via a coupled stochastic multi-plume mass flux scheme. *Mon. Weather Rev.*, https://doi.org/https://doi.org/10.1175/MWR-D-21-0215.1.

Wu, E., H. Yang, J. Kleissl, K. Suselj, M. J. Kurowski, and J. Teixeira, 2020: On the parameterization of convective downdrafts for marine stratocumulus clouds. *Mon. Weather Rev.*, **148**, 1931–1950, https://doi.org/10.1175/MWR-D-19-0292.1.

Yoshimura, H., R. Mizuta, and H. Murakami, 2015: A spectral cumulus parameterization scheme interpolating between two convective updrafts with semi-lagrangian calculation of transport by compensatory subsidence. *Mon. Weather Rev.*, **143**, 597–621, https://doi.org/10.1175/MWR-D-14-00068.1.
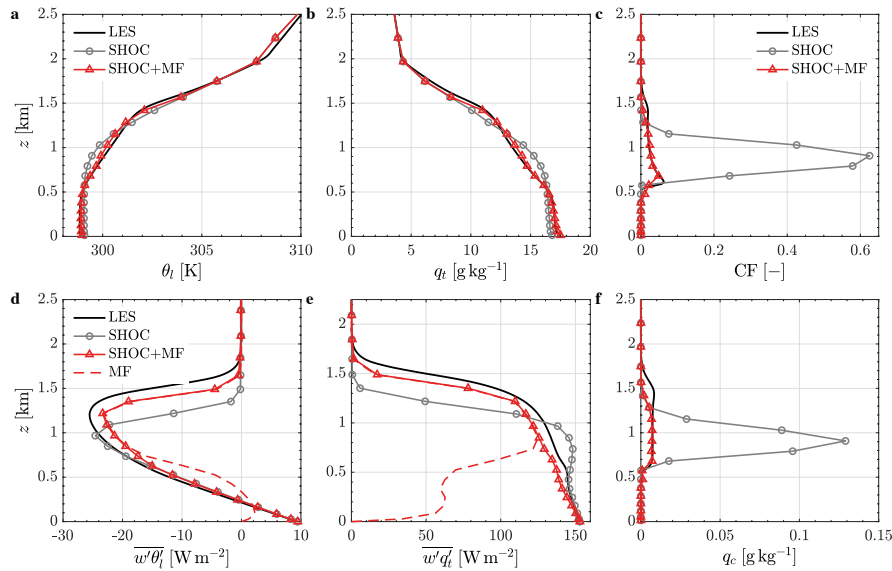
Figure 1: Vertical profiles of (a) liquid water potential temperature, (b) total water mixing ratio, (c) cloud fraction, (d) turbulent heat flux, (e) turbulent moisture flux, and (f) cloud water mixing ratio, for LES (black solid line), SHOC (solid grey line), SHOC+MF (solid red line) and MF (dashed red line) for the BOMEX case. The profiles correspond to a time average over $t = 4$–6 h.
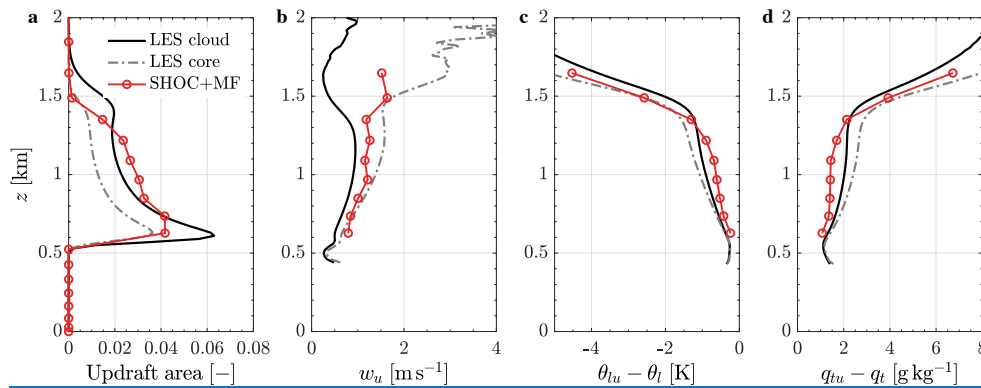
Figure 2: Vertical profiles of moist updraft properties for the BOMEX case. (a) Updraft area, (b) updraft vertical velocity, and excess relative to the grid-mean values of (c) liquid water potential temperature, $\theta_{lu} - \theta_l$, and (d) total water mixing ratio, $q_{tu} - q_t$. The solid black lines correspond to the LES cloud sampling, the dashed grey lines to the LES cloud core sampling, and the solid red lines to SHOC+MF. The profiles correspond to a time average over $t = 4$–6 h.

Figure 3: Vertical profiles of (a–d) liquid water potential temperature, and (e–h) total water mixing ratio, for LES (black solid line), SHOC (solid grey line), and SHOC+MF (solid red line) for the ARM shallow cumulus case. The legend "HH:MM LST (+X h)" shows the local standard times (LST) and the hour mark relative to the start of the simulation. The profiles correspond to hourly averages around the hour marked on each column (HH:MM LST ± 30 minutes).
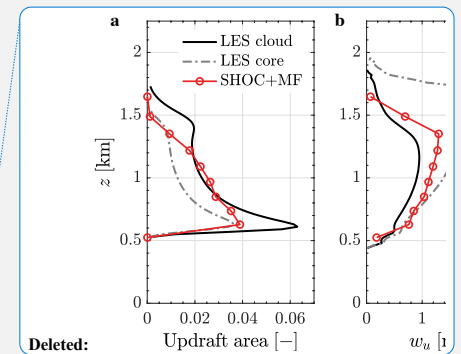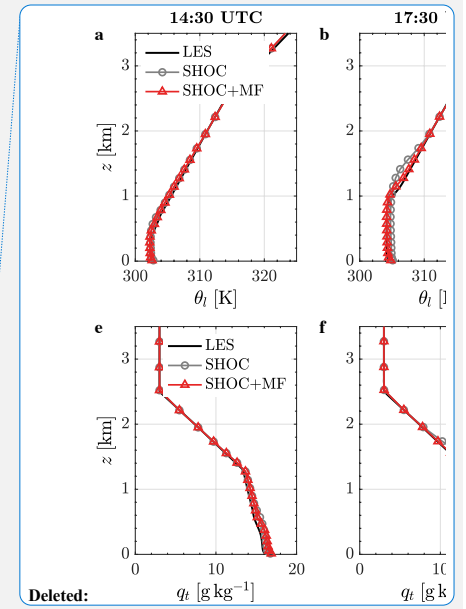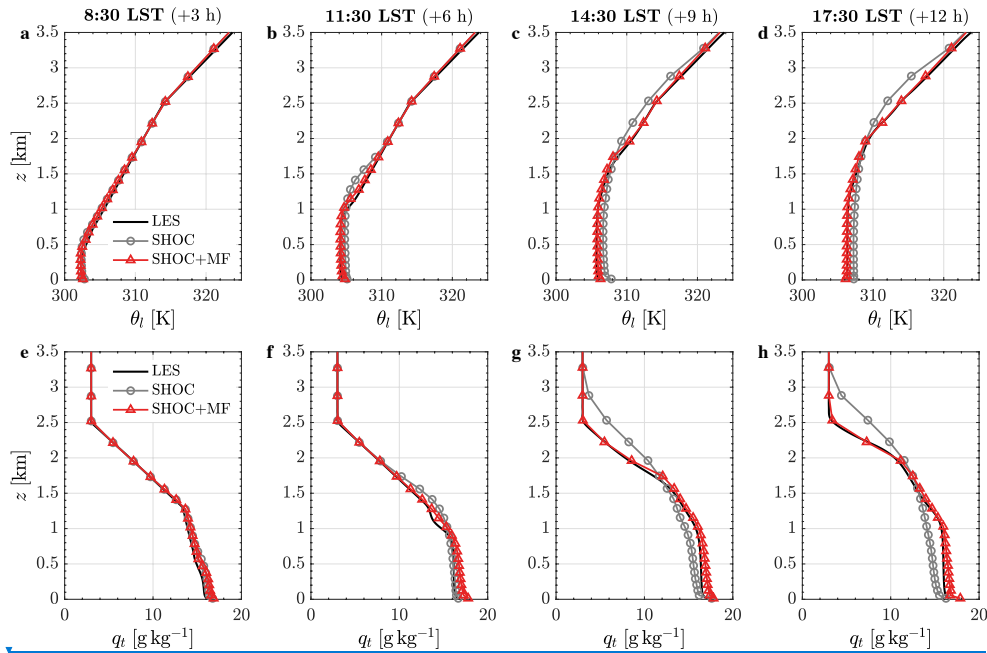
Deleted: The profiles correspond to hourly averages around the hour marked on each column (*X*:30 UTC ± 30 minutes). …
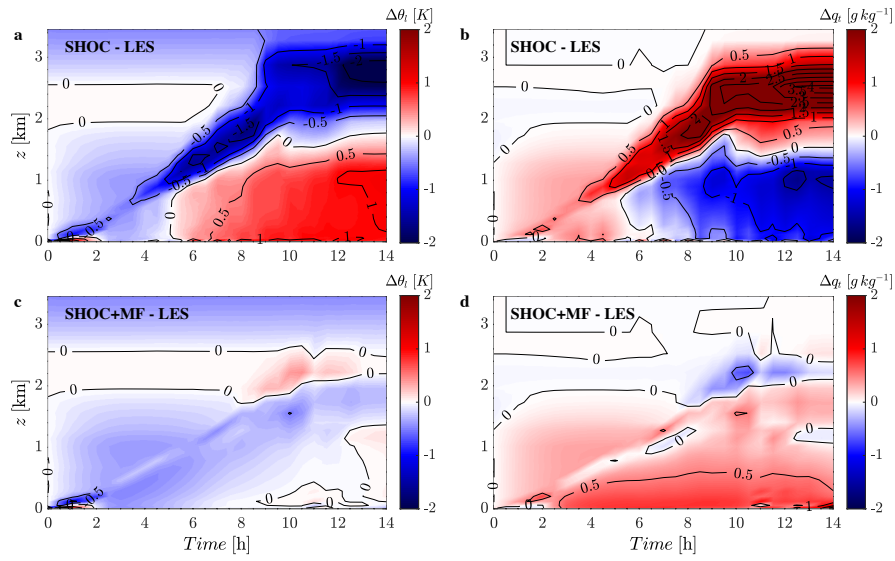
Figure 4: Time-height plot of liquid water potential temperature differences $\Delta\theta_l$ between SCM and LES for (a) SHOC, and (c) SHOC+MF, and total water mixing ratio differences Δq_t for (b) SHOC, and (d) SHOC+MF for the ARM shallow cumulus case. The LES temporal and vertical grids were interpolated to the SCREAM grids before calculating the differences.
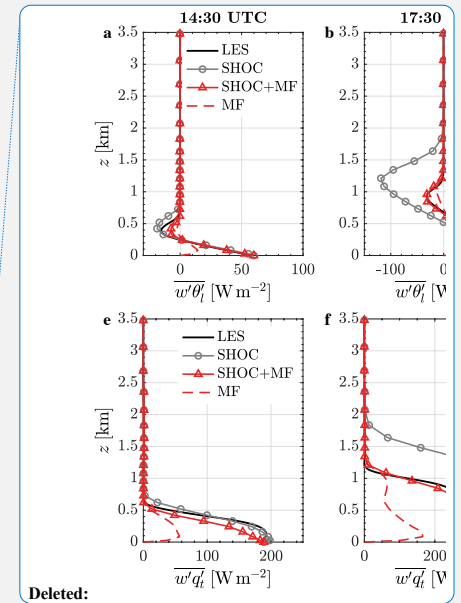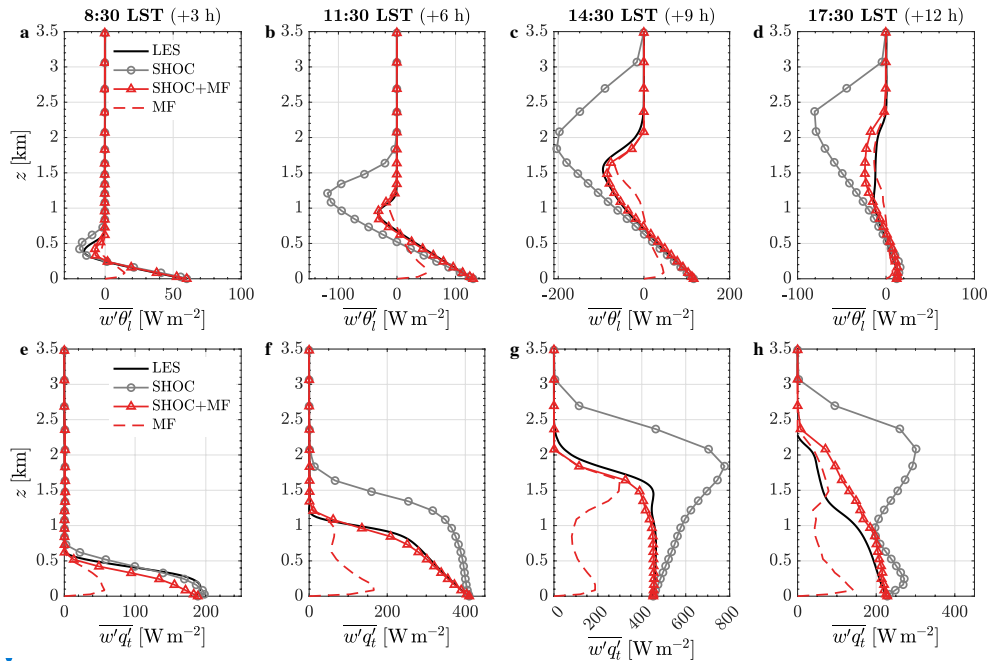
Figure 5: Vertical profiles of turbulent fluxes of (a–d) liquid water potential temperature, and (e–h) total water mixing ratio, for LES (black solid line), SHOC (solid grey line), SHOC+MF (solid red line), and MF (dashed red line) for the ARM shallow cumulus case. The legend "HH:MM LST (+X h)" shows the local standard times (LST) and the hour mark relative to the start of the simulation. The profiles correspond to hourly averages around the hour marked on each column (HH:MM LST ± 30 minutes).
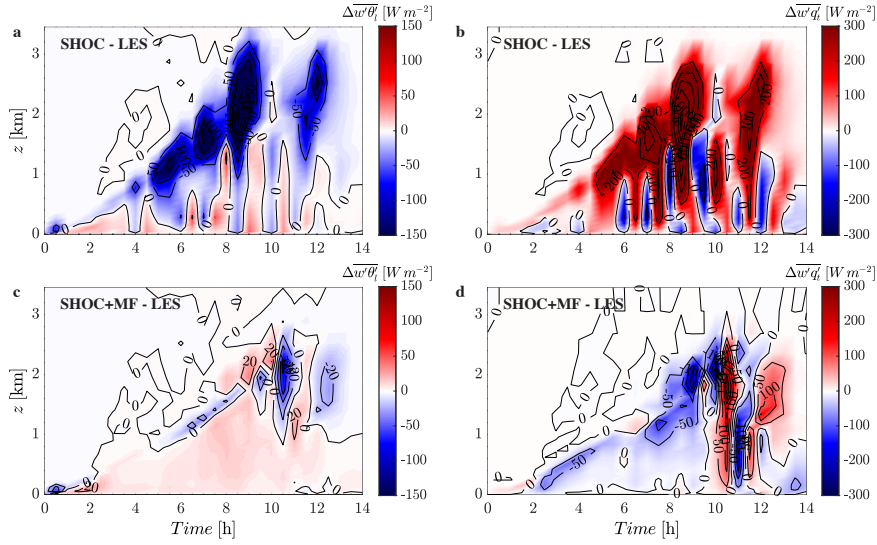
640

Figure 6: Time-height plot of liquid water potential temperature turbulent flux differences $\Delta\overline{w'\theta'_l}$ between SCM and LES for (a) SHOC, and (c) SHOC+MF, and total water mixing ratio turbulent flux differences $\Delta\overline{w'q'_t}$ for (b) SHOC, and (d) SHOC+MF for the ARM shallow cumulus case. The LES temporal and vertical grids were interpolated to the SCREAM grids before calculating the differences.
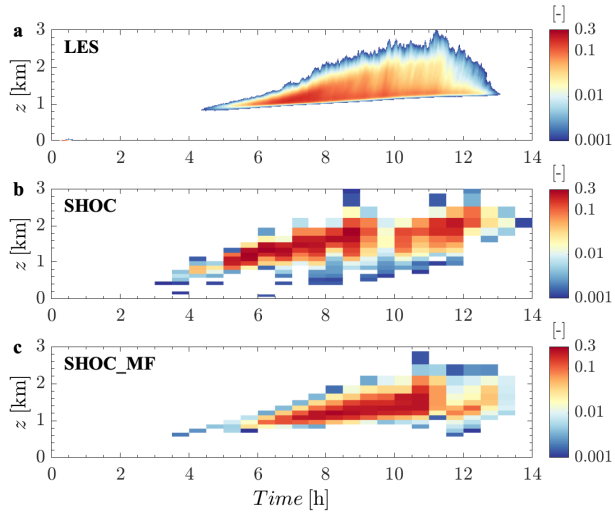
655

Figure 7: Time-height plot of (a) LES, (b) SHOC, (c) SHOC+MF cloud fraction for the ARM shallow cumulus case. The LES cloud fraction corresponds to the cloud sampling definition (i.e., $q_l > 1 \times 10^{-5}$ kg kg^{-1}). Cloud fraction values < 0.001 are masked and not plotted here.

660
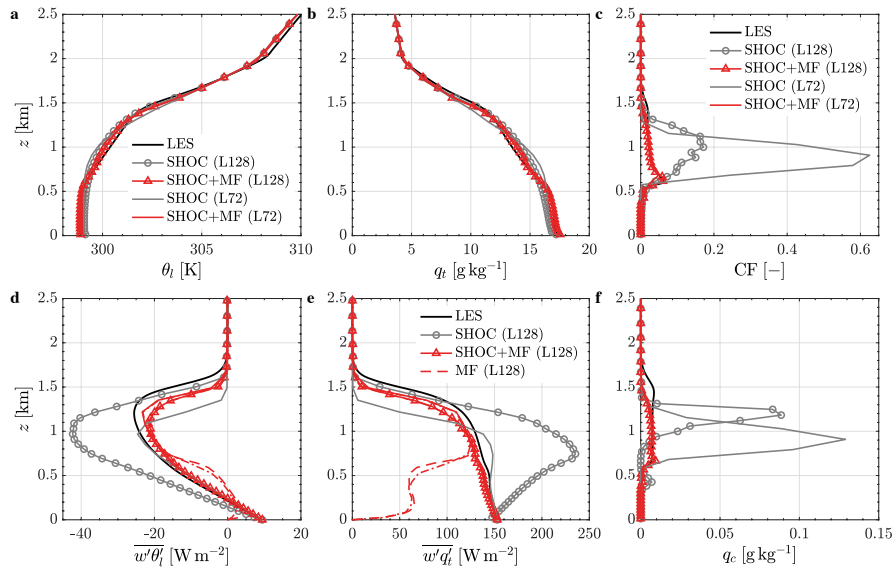
665 **Figure 8: Sensitivity of the SCM results to the vertical grid resolution for the BOMEX case. Vertical profiles of (a) liquid water potential temperature, (b) total water mixing ratio, (c) cloud fraction, (d) turbulent heat flux, (e) turbulent moisture flux, and (f) cloud water mixing ratio, for LES (black solid line), SHOC (solid grey line), SHOC+MF (solid red line) and MF (dashed red line). The high-resolution vertical grid (L128) profiles are represented by solid lines with markers (circles for SHOC and triangles for SHOC+MF), whereas the coarse-resolution vertical grid (L72) profiles are presented by plain solid lines. The dotted-dashed and dashed red profiles represent the**
670 **MF contribution using L72 and L128, respectively. The profiles correspond to a time average over $t = 4$–6 h.**
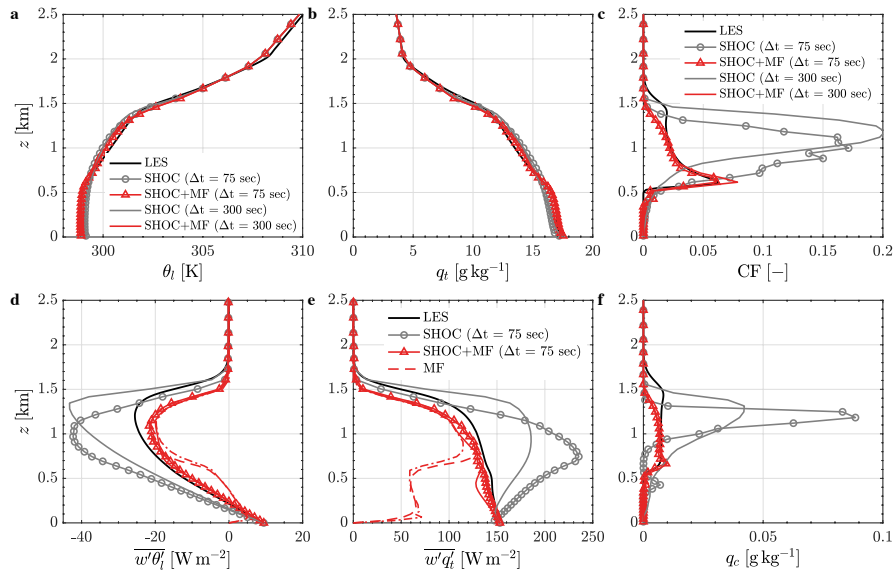
Figure 9: Sensitivity of the SCM results to the time step for the BOMEX case. Vertical profiles of (a) liquid water potential temperature, (b) total water mixing ratio, (c) cloud fraction, (d) turbulent heat flux, (e) turbulent moisture flux, and (f) cloud water mixing ratio, for LES (black solid line), SHOC (solid grey line), SHOC+MF (solid red line) and MF (dashed red line). The results obtained using $\Delta t = 75$ seconds are represented by solid lines with markers (circles for SHOC and triangles for SHOC+MF), whereas the results obtained using using $\Delta t = 300$ seconds are represented by plain solid lines. All simulations used L128 vertical grid. The profiles correspond to a time average over $t = 4$–6 h.

675